

Towards Visualizing Early-stage Osteonecrosis using Intraoperative Imaging Modalities.

Mingxu Liu^a, ✉, Alejandro Martin-Gomez^{a,b}, Julius K. Oni^c, Simon C. Mears^d,
Mehran Armand^{a,b,c,e}

^aBiomechanical- and Image-Guided Surgical Systems (BIGSS), Laboratory for Computational Sensing and Robotics, Johns Hopkins University, Baltimore, MD, USA

^bDepartment of Computer Science, Johns Hopkins University, Baltimore, MD, USA

^cDepartment of Orthopaedic Surgery, Johns Hopkins University, Baltimore, MD, USA

^dDepartment of Orthopaedic Surgery, University of Arkansas for Medical Sciences, AR, USA

^eDepartment of Mechanical Engineering, Johns Hopkins University, Baltimore, MD, USA

ABSTRACT

Osteonecrosis of the Femoral Head (ONFH) is a progressive disease characterized by the death of bone cells due to the loss of blood supply. Early detection and treatment of this disease are vital in avoiding Total Hip Replacement. Early stages of ONFH can be diagnosed using Magnetic Resonance Imaging (MRI), commonly used intra-operative imaging modalities such as fluoroscopy frequently fail to depict the lesion. Therefore, increasing the difficulty of intra-operative localization of osteonecrosis. This work introduces a novel framework that enables the localization of necrotic lesions in Computed Tomography (CT) as a step toward localizing and visualizing necrotic lesions in intra-operative images. The proposed framework uses Deep Learning algorithms to enable automatic segmentation of femur, pelvis, and necrotic lesions in MRI. An additional step performs semi-automatic segmentation of these anatomies, excluding the necrotic lesions, in CT. A final step performs pairwise registration of the corresponding anatomies, allowing for the localization and visualization of the necrosis in CT. To investigate the feasibility of integrating the proposed framework in the surgical workflow, we conducted experiments on MRIs and CTs containing early-stage ONFH. Our results indicate that the proposed framework is able to segment the anatomical structures of interest and accurately register the femurs and pelvis of the corresponding volumes, allowing for the visualization and localization of the ONFH in CT and generated X-rays, which could enable intra-operative visualization of the necrotic lesions for surgical procedures such as core decompression of the femur.

KEYWORDS

Computer Assisted Intervention; Image Guided Intervention; Deep Learning; Segmentation; Registration; Visualization

1. Introduction

Osteonecrosis of the Femoral Head (ONFH) is a progressive disease caused by the insufficient blood supply to the femoral head (Herndon and Aufranc 1972). This condition is characterized by the death of the bone cells and can lead to the collapse of the femoral head (Zhao et al. 2020). In the United States, more than 10,000 new

✉ E-mail: mliu90@jhu.edu

cases are reported each year (Aldridge 3rd and Urbaniak 2004). In other countries, such as China, the accumulated occurrence has risen to 8.12 million cases (Zhao et al. 2020). Treatments for late-stage ONFH, such as total hip replacement, usually alters or replaces the original bone anatomical structures (Petek et al. 2019). ONFH strongly threatens young adults aged 30 to 50 (Malizos et al. 2007), and with far-reaching effects: patients aged <40 years old who undergo hip replacement surgery may require to repeat the procedure more than once throughout their lifetime (Mont et al. 1996).

Core Decompression (CD) is a treatment for early-stage ONFH. This treatment requires drilling a hole in the femoral neck to access and remove the lesions in the femoral head, helping to release pressure, relieve pain, and prevent or delay the necessity of total hip replacement (Mont et al. 1996; Petek et al. 2019). During the procedure, failure to completely remove necrotic lesions or drill through the subchondral bone will result in a failed operation (Stulberg et al. 1991; Nishii et al. 2002). Determining the exact size and location of the lesions and formulating a pre-operative surgical plan is an effective way to improve the surgical outcome. In this context, Magnetic Resonance Imaging (MRI) provides the visual requirements to accurately detect pre-collapse lesions (Petek et al. 2019). However, currently available intra-operative imaging modalities in the orthopedic surgical suite, such as fluoroscopy, are not able to depict early ONFH lesions (see Fig. 1). The surgical outcome, therefore, depends on the experience and mental judgment of the surgeon when locating the lesions.

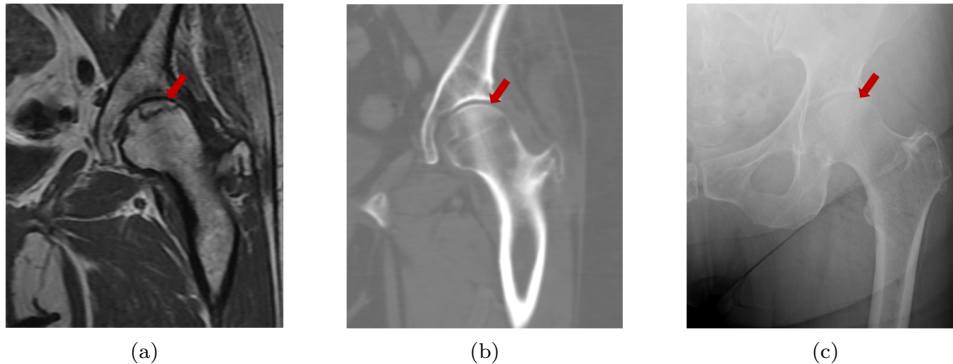


Figure 1.: Corresponding multi-modal imaging modalities of an early-stage ONFH patient. The necrotic lesion of early-stage ONFH has lower image intensities under T1 weighted MRI images (a). The observation of this lesion is hardly identifiable in other imaging modalities such as CT (b) and X-ray (c).

Although studies indicate that MRI has the potential to be used in treatment of early-stage ONFH intra-operatively, this requires renovating the operating room to be MRI compatible (Kerimaa et al. 2016). Previous work has demonstrated the great difficulty, high cost, and limitations of introducing MRI into orthopedic surgical suites (Mesko et al. 2016). To improve the accuracy of CD, studies have been conducted to fuse or transfer pre-operative data to intra-operative scenarios, using patient-specific instruments (Li et al. 2018), computer-assisted navigation systems (Theopold et al. 2020), or augmented reality (Xie et al. 2021; Wang et al. 2022). In the mentioned studies, trade-offs were made between cost, system complexity, and maintenance difficulty with the improvement of accuracy. However, to our knowledge, no previous work has attempted to improve the visualization of necrosis using intra-operative imaging modalities. Therefore, orthopedic surgeons still have no visual feedback of the necrotic

lesions during surgery.

Visualizing necrotic lesions intra-operatively may contribute to the localization during the CD procedure. Studies have demonstrated that Deep Learning (DL) is a reliable tool in helping to diagnose and process the images of femoral-related diseases. Wang et al. (Wang et al. 2021) detected the necrotic lesions using MRI, with a performance close to the experts (Wang et al. 2021). Furthermore, DL excels at segmenting proximal femurs, with an efficiency that exceeds traditional manual operation (Deniz et al. 2018).

In this work, we propose a novel framework with the potential to be seamlessly integrated as part of the surgical workflow during CD surgical procedures. To the best of our knowledge, this work represents a first step towards visualizing the early-stage ONFH for intra-operative navigation. The proposed framework can segment the anatomical bone structures in MRI and CT images, and provide means to visualize the necrotic lesion in intra-operative images. The framework, therefore, can be used to intra-operatively improve the surgical outcome of the procedures such as CD or early treatment of the ONFH. To the best of our knowledge, this work represents the first attempt towards enabling visualization of early-stage ONFH using intra-operative imaging modalities.

2. Methods

We propose a novel framework for the visualization of osteonecrosis in CT and fluoroscopic images. The proposed framework is particularly relevant during CD surgical procedures, as they frequently require the acquisition of pre-operative MRI data. This imaging modality allows observation of the early stages of necrosis and is often used for the planning of the procedure. However, integrating MRI into the orthopedic surgical suites is expensive and inefficient (Kerimaa et al. 2016). Therefore, orthopedic surgeons have to rely on intra-operative radiographic modalities for surgical guidance, which limits the discrimination and visibility of the necrotic lesions, thereby making intra-operative visualization and localization of the early-stage necrotic lesions particularly difficult.

The acquisitions of MRI and CT scans for a patient are performed at different times and locations, in which the pose of the femurs and pelvis and their spatial relationships change in MRI and CT scans. Therefore, performing segmentation on femurs and pelvis allows for estimating their poses individually and enables accurate rigid registrations. In the proposed framework, as it is depicted in Fig.2, when the pre-operative MRI is acquired, concurrent with the standardized diagnosis and staging, the image will be automatically and voxelwisely segmented into anatomical structures *in silico*. The segments contain 3D geometric information of surgical-related targets, including left and right femur, partial pelvis, and the necrotic lesion. Next, when a CT is acquired, it will be semi-automatically segmented into the femurs and partial pelvis. In the next stage, the segmented structures in MRI and CT volumes are then registered in pairs, allowing the transfer and fusion of features and plans, including the exact location and shape of the necrotic lesion extracted from the MRI.

Our long-term goal is to use fluoroscopic data with overlaid necrotic lesions as the target intra-operative image. As an intermediate step, we show that necrotic lesions can be registered to the CT volumes and projected onto synthetic X-rays. The literature documents a range of 2D-3D techniques that can facilitate the registration of CT to fluoroscopic images and complement our proposed work (Esteban et al. 2019; Grupp

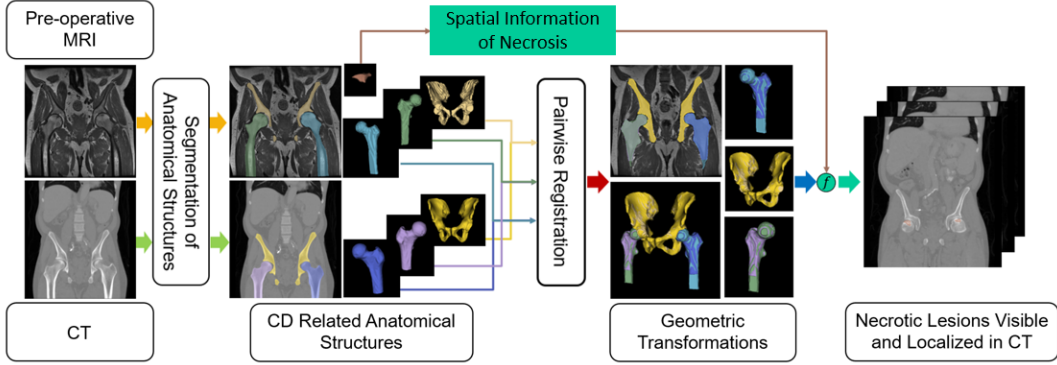


Figure 2.: The proposed framework enables segmentation of anatomical structures of interest from MRI and CT. The segmentation of these structures serves to perform registration and find the spatial transformation between imaging modalities. In which uniquely, the localization information of necrosis could only be obtained in pre-operative MRI since CT is insensitive to early-stage ONFH.

et al. 2020).

2.1. Pre-operative Image Segmentation

MRI segmentation provides voxel-level information regarding anatomical structures of interest. In addition to necrotic lesions, clear segments of the femoral structures are required in pre-operative planning. Partial pelvic structures, including the acetabulum, are also important during the pre-operative stage. Therefore, the MRI segmentation method should be able to generalize to a wide range of anatomical shapes and identify structures semantically.

In the past years, DL has shown the potential to achieve the challenges associated with identifying early stages of osteonecrosis from MRI data. In this regard, fully convolutional networks (FCNs) from nnUNet (Isensee et al. 2021), which architect on U-Net (Ronneberger et al. 2015) are developed to segment MRIs in an end-to-end manner. Given a MRI volume $X^{MRI} \in \mathbb{R}^{H \times W \times D}$, the FCNs predict a label map $\hat{Y}^{MRI} \in \mathbb{R}^{H \times W \times D}$, with multiclass voxel labels $\hat{y}^{MRI} \in \{\text{background, femur, pelvis, necrosis}\}$. H and W represent the resolution of images in coronal view. D is the number of slices along the anterior-posterior axes. As depicted in Fig. 3, the networks from nnUNet contain multiple levels of encoder-decoder blocks with skip-connection design. Four networks with variations in depth and input format are developed for side-by-side comparison. The topological structures are tabulated in Table 1. Besides the structures tabulated, a Cascade U-Net that combines the 3D low-resolution and 3D U-Nets, is developed. For all networks, the output of the first level is used as a prediction. The outputs from the remaining levels are used for Deep Supervision (Wang et al. 2015). The loss is defined by balancing cross-entropy loss and dice loss.

For the preparation of registration, a copy of the labelmap predicted by the network is then post-processed to be automatically separated into three anatomical structures as the left femur, the right femur, and the pelvis. For the voxels with label *femur* or *necrosis*, those who laying on the right of the central sagittal plane are regarded as the left femur, and vice versa.

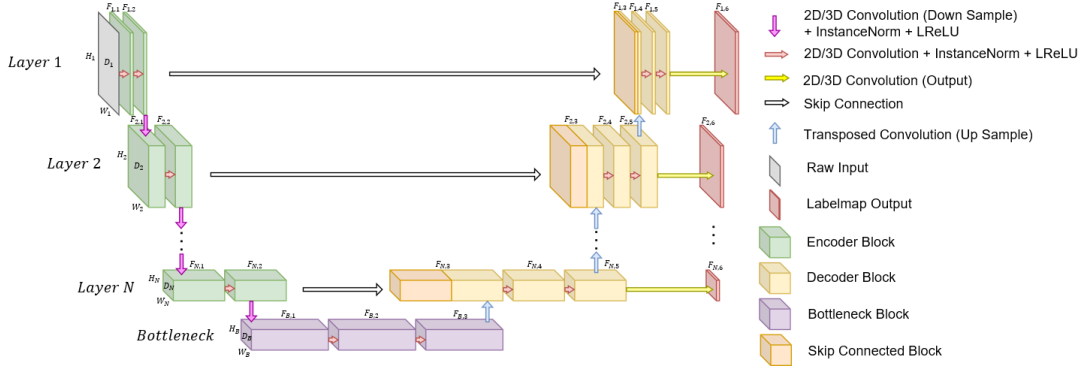


Figure 3.: The generalized architecture of MRI segmentation networks. For the convolutional operations in encoders and decoders, Instance Normalization (InstanceNorm) (Ulyanov et al. 2016) and Leaky ReLU (LReLU) (Maas et al. 2013) is used after the convolution.

Networks		U-Net 2D								U-Net 3D								U-Net 3D Low Resolution					
Layer		1	2	3	4	5	6	7	B	1	2	3	4	5	6	B	1	2	3	4	5	B	
Volume	H	640	320	160	80	40	20	10	5	256	128	64	32	16	8	4	256	128	64	32	16	8	
	W	640	320	160	80	40	20	10	5	320	160	80	40	20	10	5	256	128	64	32	16	8	
	D	1	1	1	1	1	1	1	1	20	20	20	10	5	5	5	28	28	14	7	7	7	
Encoder	F_1	32	64	128	256	480	480	480	480	32	64	128	256	320	320	320	32	64	128	256	320	320	
	F_2	32	64	128	256	480	480	480	480	32	64	128	256	320	320	320	32	64	128	256	320	320	
	F_3	64	128	256	512	960	960	960	-	64	128	256	512	640	640	-	64	128	256	512	640	-	
Decoder	F_4	32	64	128	256	480	480	480	-	32	64	128	256	320	320	-	32	64	128	256	320	-	
	F_5	32	64	128	256	480	480	480	-	32	64	128	256	320	320	-	32	64	128	256	320	-	
	F_6	4	4	4	4	4	4	4	-	4	4	4	4	4	4	-	4	4	4	4	4	-	

Table 1.: The network architectures for MRI segmentation. B indicates "bottleneck." The meaning of other symbols can be referred to in Fig.3

2.2. CT Segmentation

The segmentation of CT is used to provide accurate anatomical segments for the alignment of pre-operative segments, as well as for the propose of subsequent 2D-3D registration for intra-operative visualization. Given a CT volume $X^{CT} \in \mathbb{R}^{H \times W \times D}$, a CT segmentation model finds a $\hat{Y}^{CT} \in \mathbb{R}^{H \times W \times D}$ that predicts the label of each voxel.

In this work, CT segmentation is achieved semi-automatically following the method from Krčah et al., which is computationally fast (Krčah et al. 2011). This approach preprocesses the CT volume by enhancing the bone boundaries, then segments the volumes using a Graph-Cut segmentation framework (Boykov and Funka-Lea 2006) and empirical intensity thresholds.

Additional post-processing is required for the segmentation output to remove soft tissue and small anatomical structures, which is achieved by thresholding the volume of each labelmap. The threshold is chosen as the mean of voxel numbers of all labels. Minimal manual intervention may be conducted to prepare for the registration, including selecting and assigning relevant anatomical structures or correcting abnormal segments due to poor image quality. The resulting segmentations depict the same labels as those of the post-processed MRI (i.e., left femur, right femur, and pelvis).

2.3. Pairwise Registration of Anatomical Structures

To obtain the transformation between MRI and CT volumes of the three anatomical structures (i.e., left and right femurs, pelvis), we performed a registration stage. In this work, we use an intensity-based registration algorithm to avoid manual landmark selection and generalize to all anatomical shapes involved. Considering the rigid nature of the femur and pelvis, the registration aims to find the geometric transformations ${}^{CT}F_{MRI}^c = (R_c, t_c) \in SE(3)$, with rotation R_c and translation t_c , for every individual anatomical structures $c \in \{\text{left femur, right femur, pelvis}\}$ such that:

$${}^{CT}F_{MRI}^c = \arg \max_{{}^{CT}F_{MRI}^c} S \left({}^{CT}F_{MRI}^c(\hat{Y}_n^{CT,c}), \hat{Y}_n^{MRI,c} \right) \quad (1)$$

Where S is the similarity metric, and $\hat{Y}_n^{CT,c}$ is the CT labelmap predicted and post-processed by the method in Section 2.2, $\hat{Y}_n^{MRI,c}$ is the MRI label map predicted and post-processed by the method in Section 2.1. The objective is to maximize image similarity between the MRI image and the transformed CT image.

The transformation from MRI to CT can be derived by inverting the transformation:

$${}^{MRI}F_{CT}^c = (R_c^{-1}, -R_c^{-1}t_c) \quad (2)$$

The algorithm proposed by Johnson et al. is used for the optimization procedure (Johnson et al. 2007). The MRI segments are set as the fixed volume, and the CT segments as the moving volume. Mutual Information is used as the similarity metric S . An initial transformation that moves CT segments close to MRI segments is essential to avoid local minima and improve efficiency. In this work, considering femurs and pelvis are rigid objects, and the fact that the major difference in MRI and CT poses comes from the translational term t_c , the initial estimation is set as alignment of volume mass center. Manual alignment is allowed but not necessary unless the optimization process encounters extreme local minima. With the appropriate registration, the segments and features in MRI volume can be transformed into the space of corresponding CT volumes using the inverse transformation indicated in Eq.2. Due to the difference in volume spacing between MRI and CT images, the transferred segments and features are re-sampled using BSpline interpolation to depict similar volume spacing as the CT.

3. Experiments and Preliminary Results

To evaluate the performance of the segmentation and registration stages of the proposed framework, we conducted an experiment using the MRI and CT images of early-stage ONFH patients who qualified for the CD procedure. Our dataset consisted of 20 MRI volumes, from which six of them contained corresponding CT data. All volumes were taken along the coronal view. For MRI, eighteen volumes corresponded to T1-weighted sequences, and the remaining two volumes were short tau inversion recovery (STIR) series. Depending on the patients, the sizes of the voxels varied from $0.43 \times 0.43 \text{mm}^2$ to $0.86 \times 0.86 \text{mm}^2$, with coronal spacings from 3.3mm to 7.2mm . MRIs were manually annotated with the assistance of an orthopedic surgeon. The annotation contained three anatomical structures: {femur; pelvis, necrosis}. The intra-operative CTs had in-plane voxel size ranging from $0.83 \times 0.83 \text{mm}^2$ to $1 \times 1 \text{mm}^2$, and coronal

spacing ranging from $0.5mm$ to $3mm$.

3.1. MRI and CT Segmentation

We trained and tested the MRI segmentation networks on the 20 volumes collected. The training and validation were conducted with nnUNet (Isensee et al. 2021) using specific configurations explained as follows. The dataset was divided into five subsets with equal numbers of volumes, and five-fold cross-validations were performed. The models were optimized with Adam optimizer, with an initial learning rate of 1×10^{-2} and learning rate scheduler enabled. For the 2D U-Net, we used a batch size of 8. For U-Net (3D), U-Net (3D low resolution), and Cascade U-Net, we used a batch size of 2.

The MRI volumes were resampled to have the medium spacing of the dataset. The intensities of voxels were normalized and fed into the networks. Bi- or three-dimensional elastic deformation and image rotation were enabled as data augmentation. To avoid overfitting, and based on the average converging epoch numbers of networks, 2D UNet, 3D UNet, and 3D low-resolution UNet were trained for 100 epochs, and 3D cascade UNet were trained for 150 epochs. The training was conducted on Nvidia RTX 2080Ti. Each epoch took 150-210 seconds for training and validation. The latest model and the one with the best performance on the validation data set were saved.

Models were evaluated on the basis of accuracy, dice score, precision, and recall. Table 2 shows the summary of the validation performances of the latest model in each fold. The outputs from the networks of one MRI sample are illustrated in Fig. 4. Although the proposed models showed comparable performance, the Cascade U-Net produced the lowest number of false positive and false negative predictions on segmentation. In addition, it produced the most well-defined segmentation of the anatomy (see Fig.5). Furthermore, despite Cascade U-Net being more complex, the computational load resulting from this model is comparable to the others. Therefore, Cascade U-Net was selected as the final MRI segmentation model for the proposed network. The outputs of the network were then post-processed with the method stated in Section 2.1. The CT volume paired with the MRI was also segmented and post-processed. All six CT volumes were successfully segmented. The result is illustrated in Fig.6. The segmentation accuracy of CT was not evaluated individually, as it had been previously validated by Krčah et al. (Krčah et al. 2011).

3.2. Experiment and Example on framework Performance

The corresponding segments of the six patients with paired MRI and CT volumes obtained from Section 3.1 were used for registration. All segments were successfully registered. Three rigid transformations (i.e., one for the left femur, one for the right femur, and one for the pelvis) for each patient were obtained. No manual alignment was performed for the 12 pairs of femurs and six pairs of pelvis. The registration result is presented in Fig. 7.

No landmarks were required on CT and MRI volumes for this framework. Therefore, we evaluated the registration based on images. In addition, the intensity difference between MRI and CT could strongly bias the results of traditional image similarity metrics. Therefore, we evaluated how well the anatomical segments from MRI and CT images are overlaid after registration (Balakrishnan et al. 2019). Following the method

Model	Class	Accuracy	Dice Score	Precision	Recall
		$\frac{TP+TN}{TP+TN+FP+FN}$	$\frac{2 \times TP}{2 \times TP+FP+FN}$	$\frac{TP}{TP+FP}$	$\frac{TP}{TP+FN}$
2D U-Net	Femur	1.00±0.00	0.92±0.03	0.93±0.02	0.92±0.05
	Pelvis	0.99±0.00	0.90±0.04	0.93±0.02	0.88±0.07
	Necrosis	1.00±0.00	0.59±0.25	0.72±0.31	0.63±0.20
3D Full Res U-Net	Femur	1.00±0.00	0.93±0.03	0.93±0.03	0.92±0.05
	Pelvis	0.99±0.00	0.91±0.03	0.92±0.02	0.90±0.06
	Necrosis	1.00±0.00	0.60±0.27	0.67±0.29	0.66±0.21
3D Low Res U-Net	Femur	1.00±0.00	0.92±0.03	0.93±0.03	0.92±0.04
	Pelvis	0.99±0.00	0.91±0.03	0.92±0.02	0.90±0.05
	Necrosis	1.00±0.00	0.57±0.27	0.65±0.29	0.64±0.23
3D Cascade U-Net	Femur	1.00±0.00	0.93±0.03	0.93±0.03	0.93±0.05
	Pelvis	1.00±0.00	0.91±0.03	0.92±0.02	0.91±0.05
	Necrosis	1.00±0.00	0.59±0.28	0.67±0.29	0.65±0.22

Table 2.: Statistical results of MRI segmentation, arranged in mean and standard derivatives. TP = True Positive, TN = True Negative, FP = False Positive, FN = False Negative.

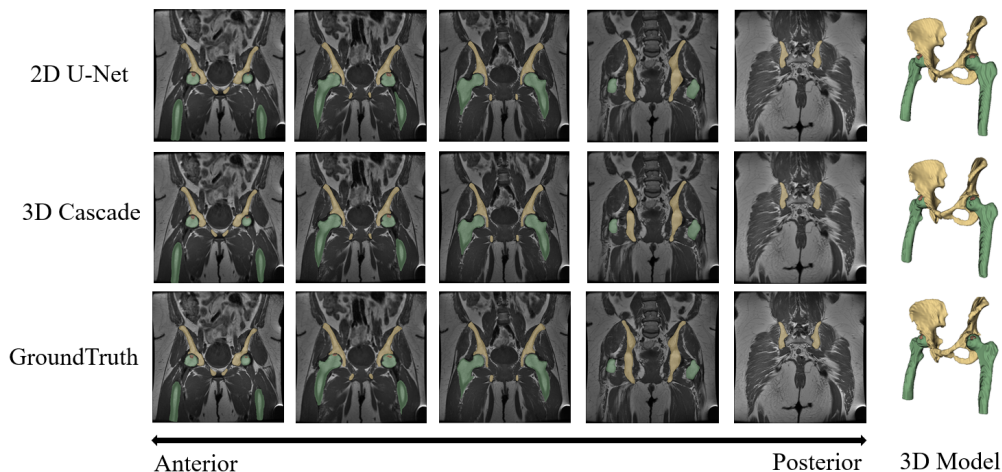


Figure 4.: The performances of 2D UNet and 3D Cascade UNet comparing to the ground truth.

described in Section 2.3, we transferred and re-sampled the anatomical labelmaps, including left/right femurs and pelvis, from MRI space to CT space, resulting in a labelmap containing $({}^{CT}F_{MRI}^c)^{-1}\hat{Y}^{MRI,c}$ for $c \in \{\text{left femur, right femur, pelvis}\}$.

Defining $\hat{Y}^{CT,c}$ as the ground truth of a patient’s anatomical segmentation, the performance of the registration in the proposed framework was evaluated by how well the transformed prediction $({}^{CT}F_{MRI}^c)^{-1}\hat{Y}^{MRI,c}$ matched the target $\hat{Y}^{CT,c}$. Dice Score was used as the indicator of the similarity between $\hat{Y}^{CT,c}$ and $({}^{CT}F_{MRI}^c)^{-1}\hat{Y}^{MRI,c}$. Results of the femurs registration have an average dice score of 0.81, and a range of [0.74,0.86]. For the pelvis, the registrations have an average dice score of 0.81, and a range of [0.77,0.87].

After registration, we applied our framework by transferring the necrotic data onto the CT volumes. As an application example of the proposed framework, the necrosis detected in MRI volume was automatically segmented and visualized in its corresponding CT (see Fig.8).



Figure 5.: 3D Cascade U-Net (a) provided segmentation with well-defined anatomical structures comparing to 2D U-Net (b).

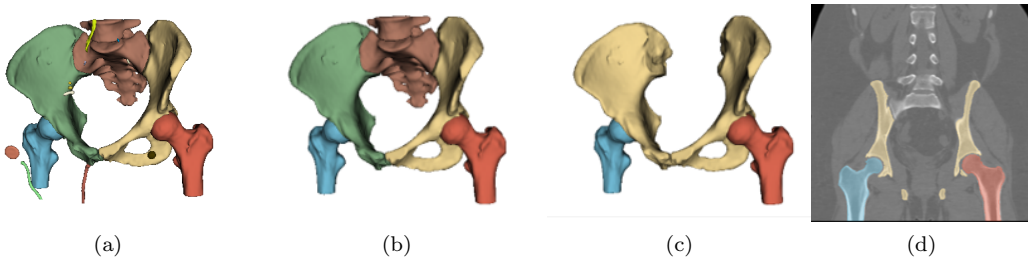


Figure 6.: (a): the initial CT segmentation; (b): the CT segmentation by filtering out soft tissues; (c) and (d): the final CT segmentation with correct labels and removal of irrelevant bone anatomies.

Furthermore, we used digitally reconstructed radiographs (DRR) to generate synthetic x-rays from the CT volumes. The generation of these images has proven valuable in performing 2D/3D registration of femurs/pelvis (Grupp et al. 2020; Esteban et al. 2019). In this work, we used DeepDRR (Unberath et al. 2018) to generate our synthetic X-rays. We used the camera parameters of a Siemens CIOS Fusion to generate the synthetic fluoroscopic images from the CT volumes in our dataset (see Fig. 9a). However, because of the imaging capabilities of the CT volume, synthetic fluoroscopic images are not able to depict necrotic lesions. Therefore, to enable the visualization of the necrosis, we transferred and localized the lesions in the CT by applying our proposed framework. We regarded the necrosis as high-density material which caused high attenuation on synthetic X-rays. By combining the necrosis extracted from the MRI into the DRR projection, we were able to localize and visualize necrotic lesions in fluoroscopic images (see Fig. 9b and Fig. 9c). Furthermore, in addition to enabling visualization of the necrosis in the fluoroscopic images, the results of the proposed framework could be used to enable 2D-3D registration and provide visual assistance for orthopedic surgeons.

4. Discussion

The experimental results presented in this work show that the proposed framework allows for the observation and localization of necrotic tissue using CT scans. We have also shown that the proposed framework enables the visualization of the necrotic tissue

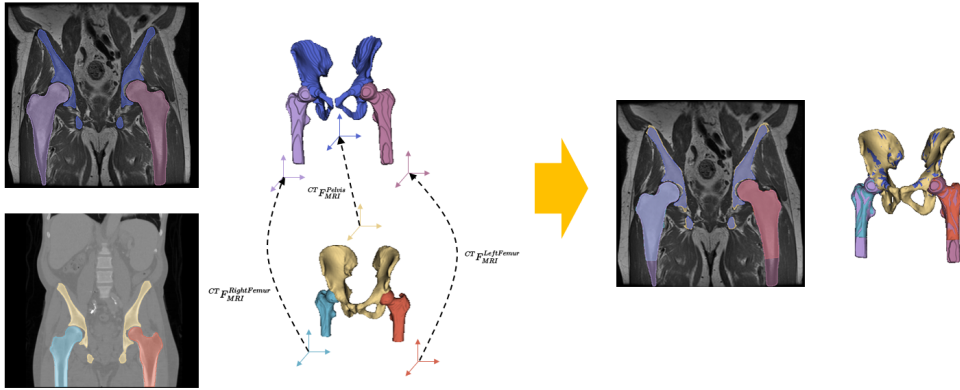


Figure 7.: The MRI image slice, CT image slice, and 3D model without registration are on the left. Where on the right of the arrow are the MRI image slice and 3D model with proper registration. The necrosis is merged into the femurs for registration.

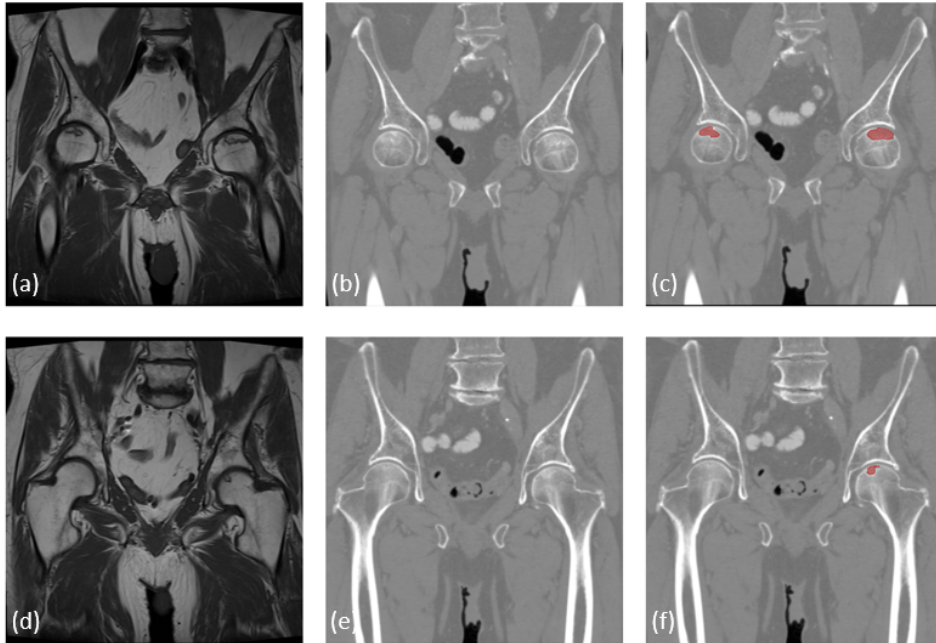


Figure 8.: This figure shows an application of the proposed framework. In (a) and (d), the necrotic lesions are identifiable in MRI scans. On the contrary, the necrotic lesions cannot be localized in CT scans (b) and (e). (c) and (f) show an application of our framework where we made the necrotic lesion visible (in red) on CT scans.

using synthetic X-rays. This feature will further allow the application of established 2D-3D techniques to enable navigation capabilities and further assist orthopedic surgeons during the performance of the CD procedures. The proposed method is low cost, requires no additional training for orthopedists, and it has the potential to be integrated into the current surgical workflow. Moreover, to the best of our knowledge, this work represents the first attempt towards enabling visualization of early-stage ONFH

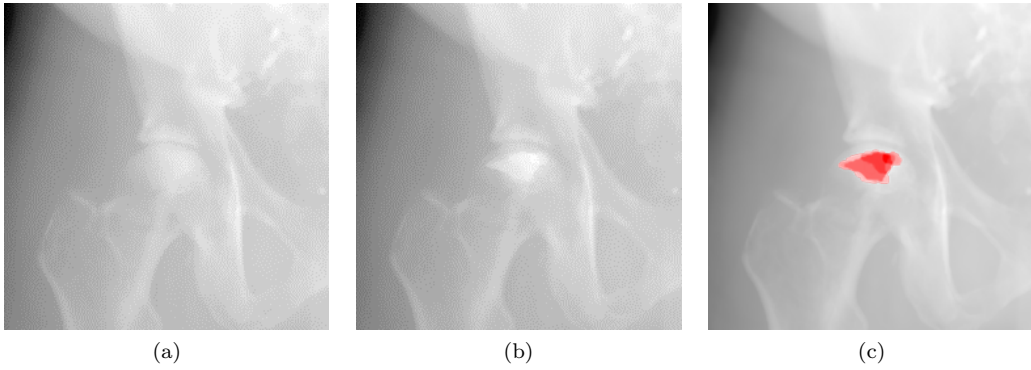


Figure 9.: A digitally reconstructed radiograph generated from a CT (a) is enhanced by depicting the necrotic lesion using the proposed framework (b). These results are highlighted by adding colored augmentations to the original results (c).

using intra-operative image modalities.

The evaluation metrics and the visualizations in the experiment indicate that the MRI segmentation network is capable of segmenting the femur and relevant pelvic structures. The fully automatic and end-to-end segmentation could significantly reduce the processing time compared to the traditional manual segmentation of MRI.

The prediction error in pelvis and femur segmentation mainly comes from the dark black voxels in the structures. Dark black voxels in T1 weighted MRI indicate insufficient local resonance signals are received, which could be associated with cortical bone anatomy, air, (Caldemeyer and Buckwalter 1999), or undesired artifacts, which may not be distinguishable by the proposed models.

For the segmentation of early-stage necrotic lesions, our model has a good and sensitive segmentation effect for those with prominent characteristics, typically referring to single hyperdense lines under T1 weight MRI (Petek et al. 2019). The model performance is less stable for osteonecrosis that develops irregularly. This phenomenon is also reflected in related work, including (Wang et al. 2021). At the same time, we also noticed that the MRI artifacts are very likely to appear at the location of the femoral head (see Fig. 10), which could also affect the performance of the segmentation model.



Figure 10.: An example of artifact on left femoral head.

The excessively small size of necrosis is another important factor that hinders MRI segmentation performance. The small size of the lesions causes the Dice Score to

be more sensitive to small changes in predictions. In addition, the spacing used for acquiring the MRI in our dataset only allows the necrotic lesions to be visible on a few slices. The reduced size of the necrotic lesions combined with the limited image slices available complicates network learning. Moreover, the specificity of the target patient population and the challenges associated with acquiring a dataset containing paired data play an even more profound effect on the segmentation of osteonecrosis. In this regard, we believe that the performance of the models presented in this work would significantly benefit from the availability of a larger dataset containing this type of lesion.

The effect of segmentation for necrosis does not affect the framework to function properly. In fact, the automatic segmentation of necrosis provides a solid initial estimate for the diagnosis and localization of ONFH. The refinement of the necrotic lesion segmentation could be done simultaneously when orthopedists diagnose and plan the surgery on pre-operative images, which is not a tedious or complicated procedure since the necrosis is small and well-characterized.

Our results show that the proposed framework can achieve reliable registration between MRI and CT volumes after the segmentation stages. During the experiment, due to the significant difference between MRI and CT intensity, conventional image similarity metrics fail to reflect the change of registration effect very sensitively. The evaluation metric used in this work is not based on image intensity and can reflect changes in registration effects. The average dice scores for the registration of femurs and pelvis are 0.81, which are in line with the alignment that can be visually perceived. Statistics also show that the framework performs very well in different patient data. This shows the stability and effectiveness of our framework.

We noticed the evaluation metric used to measure registration also accumulates the error from segmentation. Target Registration Error (TRE) is generally a more straightforward metric for measuring the registration effect. However, TRE requires the professional annotation of landmarks, which is not a prerequisite for the proposed purely image-based method. Moreover, since the necrotic lesion is not identifiable in CT or fluoroscopic images, the available scheme to evaluate segmentation and registration performance on necrotic lesions is limited. In this regard, we expect that additional MRI images acquired at the same pose as the CT would support the generation of ground truth data to improve the validation of the proposed framework.

Due to the differences in spacing observed between MRIs and CTs, we used B-Spline interpolation to mathematically approximate the shape of the necrotic lesion and represented it in the CT volume. The interpolation may deviate the position and shape of the necrotic lesion from the actual one. This problem can be greatly alleviated by the acquisition of MRI and CT volumes with similar spacing.

We believe that the framework is also highly extendable. In the experiment, we visualized the necrotic lesions in a 3D imaging modality using 3D-3D registration. We also showed that the necrotic lesion could be transferred and projected into synthetic fluoroscopic images using DRR, potentially enabling the integration of the proposed framework with 2D-3D registration algorithms (Esteban et al. 2019; Grupp et al. 2020).

5. Conclusion

In this work, we presented a novel framework for Core Decompression surgery, which allows for intra-operative visualization of early-stages ONFH using CT scans and digitally reconstructed radiographs. This framework has the potential to segment the

necrotic lesions from pre-operative volumes and enables intra-operative visualization of the lesions using fluoroscopic images. The proposed framework combines medical image segmentation and registration algorithms to achieve a seamless transfer of pre-operative features and plans to intra-operative scenarios. In the experiment, we successfully localized and visualized osteonecrosis on the CT images and synthetic fluoroscopic images.

Acknowledgements

This research was partially supported by NIH grants R01EB023939 and R01EB016703.

References

- Aldridge 3rd JM, Urbaniak JR. 2004. Avascular necrosis of the femoral head: etiology, pathophysiology, classification, and current treatment guidelines. *American journal of orthopedics* (Belle Mead, NJ). 33(7):327–332.
- Balakrishnan G, Zhao A, Sabuncu MR, Guttag J, Dalca AV. 2019. Voxelmorph: a learning framework for deformable medical image registration. *IEEE transactions on medical imaging*. 38(8):1788–1800.
- Boykov Y, Funka-Lea G. 2006. Graph cuts and efficient nd image segmentation. *International journal of computer vision*. 70(2):109–131.
- Caldemeyer KS, Buckwalter KA. 1999. The basic principles of computed tomography and magnetic resonance imaging. *Journal of the American Academy of Dermatology*. 41(5):768–771.
- Deniz CM, Xiang S, Hallyburton RS, Welbeck A, Babb JS, Honig S, Cho K, Chang G. 2018. Segmentation of the proximal femur from mr images using deep convolutional neural networks. *Scientific reports*. 8(1):1–14.
- Esteban J, Grimm M, Unberath M, Zahnd G, Navab N. 2019. Towards fully automatic x-ray to ct registration. In: *International Conference on Medical Image Computing and Computer-Assisted Intervention*. Springer. p. 631–639.
- Grupp RB, Unberath M, Gao C, Hegeman RA, Murphy RJ, Alexander CP, Otake Y, McArthur BA, Armand M, Taylor RH. 2020. Automatic annotation of hip anatomy in fluoroscopy for robust and efficient 2d/3d registration. *International journal of computer assisted radiology and surgery*. 15(5):759–769.
- Herndon JH, Aufranc OE. 1972. Avascular necrosis of the femoral head in the adult: a review of its incidence in a variety of conditions. *Clinical Orthopaedics and Related Research*®. 86:43–62.
- Isensee F, Jaeger PF, Kohl SA, Petersen J, Maier-Hein KH. 2021. nnu-net: a self-configuring method for deep learning-based biomedical image segmentation. *Nature methods*. 18(2):203–211.
- Johnson H, Harris G, Williams K. 2007. Brainsfit: Mutual information registrations of whole-brain 3d images, using the insight toolkit.
- Kerimaa P, Väänänen M, Ojala R, Hyvönen P, Lehenkari P, Tervonen O, Blanco Sequeiros R. 2016. Mri-guidance in percutaneous core decompression of osteonecrosis of the femoral head. *European radiology*. 26(4):1180–1185.
- Krčah M, Székely G, Blanc R. 2011. Fully automatic and fast segmentation of the femur bone from 3d-ct images with no shape prior. In: *2011 IEEE International Symposium on Biomedical Imaging: From Nano to Macro*. p. 2087–2090.
- Li B, Lei P, Liu H, Tian X, Wen T, Hu R, Hu Y. 2018. Clinical value of 3d printing guide plate in core decompression plus porous bioceramics rod placement for the treatment of early osteonecrosis of the femoral head. *Journal of Orthopaedic Surgery and Research*. 13(1):1–7.

- Maas AL, Hannun AY, Ng AY, et al. 2013. Rectifier nonlinearities improve neural network acoustic models. In: Proc. icml; vol. 30. Atlanta, Georgia, USA. p. 3.
- Malizos KN, Karantanas AH, Varitimidis SE, Dailiana ZH, Bargiotas K, Maris T. 2007. Osteonecrosis of the femoral head: Etiology, imaging and treatment. *European Journal of Radiology*. 63(1):16–28. *Hip Joint*; Available from: <https://www.sciencedirect.com/science/article/pii/S0720048X07001593>.
- Mesko NW, Joyce DM, Ilaslan H, Joyce MJ. 2016. Creating an intraoperative mri suite for the musculoskeletal tumor center. *Clinical Orthopaedics and Related Research*®. 474(6):1516–1522.
- Mont MA, Carbone JJ, Fairbank AC. 1996. Core decompression versus nonoperative management for osteonecrosis of the hip. *Clinical Orthopaedics and Related Research*®. 324:169–178.
- Nishii T, Sugano N, Ohzono K, Sakai T, Sato Y, Yoshikawa H. 2002. Significance of lesion size and location in the prediction of collapse of osteonecrosis of the femoral head: a new three-dimensional quantification using magnetic resonance imaging. *Journal of orthopaedic research*. 20(1):130–136.
- Petek D, Hannouche D, Suva D. 2019. Osteonecrosis of the femoral head: pathophysiology and current concepts of treatment. *EFORT Open Reviews*. 4(3):85 – 97. Available from: <https://eor.bioscientifica.com/view/journals/eor/4/3/2058-5241.4.180036.xml>.
- Ronneberger O, Fischer P, Brox T. 2015. U-net: Convolutional networks for biomedical image segmentation.
- Stulberg B, Davis A, Bauer T, Levine M, Easley K. 1991. Osteonecrosis of the femoral head. a prospective randomized treatment protocol. *Clinical orthopaedics and related research*. (268):140–151. Available from: <http://europepmc.org/abstract/MED/2060201>.
- Theopold J, Armonies S, Pieroh P, Hepp P, Roth A. 2020. Nontraumatic avascular necrosis of the femoral head. *Operative Orthopädie und Traumatologie*. 32(2):107–115.
- Ulyanov D, Vedaldi A, Lempitsky V. 2016. Instance normalization: The missing ingredient for fast stylization. arXiv preprint arXiv:160708022.
- Unberath M, Zaech JN, Lee SC, Bier B, Fotouhi J, Armand M, Navab N. 2018. Deepdrr—a catalyst for machine learning in fluoroscopy-guided procedures. In: *International Conference on Medical Image Computing and Computer-Assisted Intervention*. Springer. p. 98–106.
- Wang L, Lee CY, Tu Z, Lazebnik S. 2015. Training deeper convolutional networks with deep supervision. arXiv preprint arXiv:150502496.
- Wang P, Liu X, Xu J, Li T, Sun W, Li Z, Gao F, Shi L, Li Z, Wu X, et al. 2021. Deep learning for diagnosing osteonecrosis of the femoral head based on magnetic resonance imaging. *Computer Methods and Programs in Biomedicine*. 208:106229.
- Wang Q, Ding R, Yao Y, Pan J, Wang W. 2022. Augmented reality navigation-guided core decompression for osteonecrosis of femoral head. *Journal of Visualized Experiments: Jove*. (182).
- Xie D, Xue W, He J, Luo Y, Wang X, Yan Z. 2021. A small-scaled intraoperative 3d visualization navigation system for femoral head repair surgery. In: *2021 6th International Conference on Image, Vision and Computing (ICIVC)*. p. 328–335.
- Zhao D, Zhang F, Wang B, Liu B, Li L, Kim SY, Goodman SB, Hernigou P, Cui Q, Lin-eaweaver WC, et al. 2020. Guidelines for clinical diagnosis and treatment of osteonecrosis of the femoral head in adults (2019 version). *Journal of orthopaedic translation*. 21:100–110.